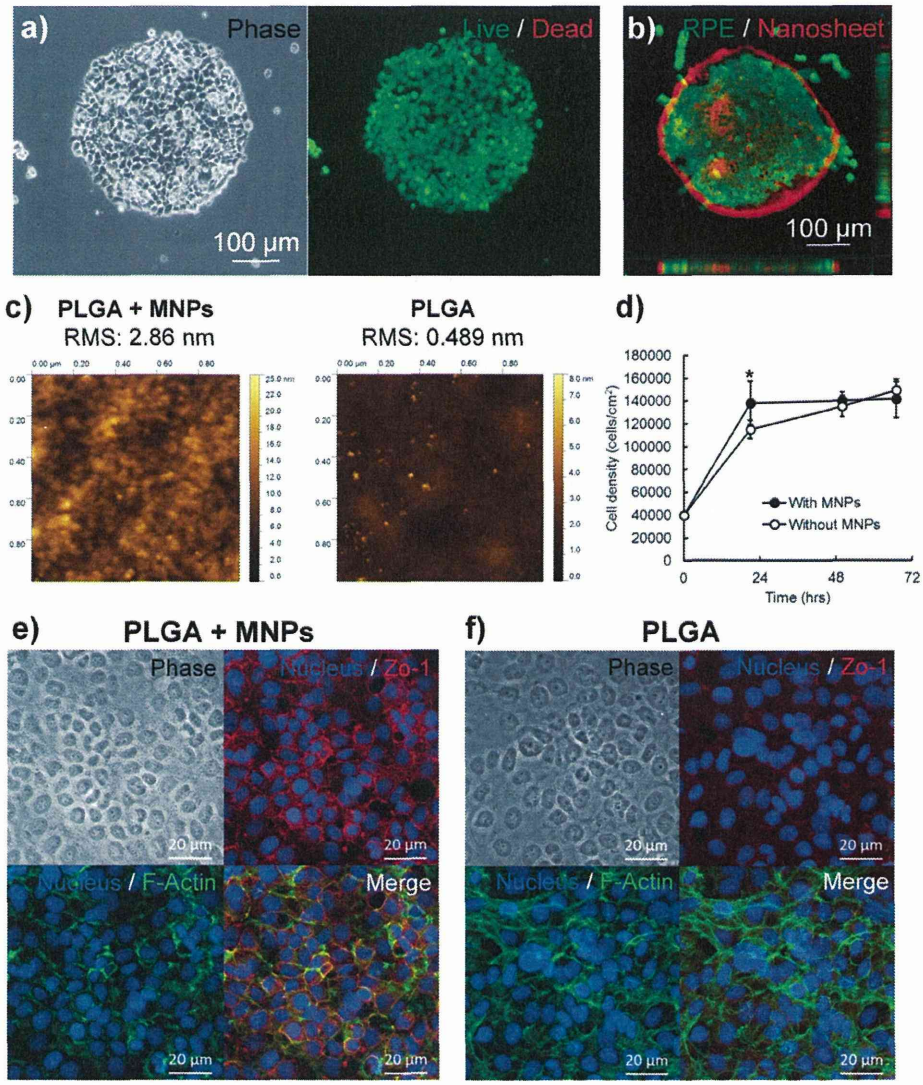

Figure 2. Micropatterned nanosheets direct RPE-J cellular morphogenesis. a) RPE-J cells on micropatterned nanosheets (400 µm ϕ) after 1 d of culture stained to show live/dead cells. b) A CLSM image showing monolayer formation by the RPE-J cells on the nanosheet (stained with rhodamine B). c) AFM surface morphology of micropatterned PLGA nanosheets with and without MNPs. d) Influence of MNPs on the proliferation of RPE-J cells. Immunostaining of the RPE monolayer on the nanosheet e) with and f) without MNPs (top left, phase microscopy; top right, nucleus and tight junction protein ZO-1; bottom left, nucleus and F-actin; bottom right, merged image). On the MNP surface, the RPE-J cells showed bridges among the ZO-1 tight junctions with hexagonal structures. Student *t*-test with $^*p < 0.05$ set as the level of statistical significance.

cells showed that the RPE-J cells adhered to the micropatterned nanosheet and remained viable; no adherent cells were observed outside the nanosheet due to the swelling of the PVA layer (**Figure 2**a). We then analyzed cellular organization using a confocal laser scanning microscope (CLSM) to determine whether the RPE-J cells formed a monolayer. CLSM images clearly showed monolayer formation by the RPE-J cells (colored green by calcein AM) on the micropatterned nanosheet (colored red by rhodamine B) (Figure 2b). Also, the rim of the nanosheet (see Figure S3, Supporting Information) was clearly observed in the CLSM image. The RPE monolayer formed consistently across the nanosheet, as confirmed by cross-sectional images. In addition to monolayer formation, RPE cells formed a densely packed structure (a "cobblestone-like" morphology) that is critical for their ability to function as a barrier under physiological conditions.[12] It has been reported that the nanostructured surface generated by nanoparticles or by means of electron beam lithography has a significant impact on cell proliferation or cytoskeletal organization at the nanoscale.[13] Thus, we sought to influence RPE cell morphogenesis by modulating the surface structure of the nanosheets with MNPs. Atomic force microscope (AFM) measurements revealed that the inclusion of MNPs generated a rough surface (Figure 2c); the surface roughness (root-mean-squared value) was increased by more than 5 times by the inclusion of MNPs from 0.489 nm ([MNPs] = 0 mg mL^{-1}) to 2.86 nm ([MNPs] = 2.5 mg mL^{-1}).

ADVANCED MATERIALS
www.advmat.de

Materials Views
www.MaterialsViews.com

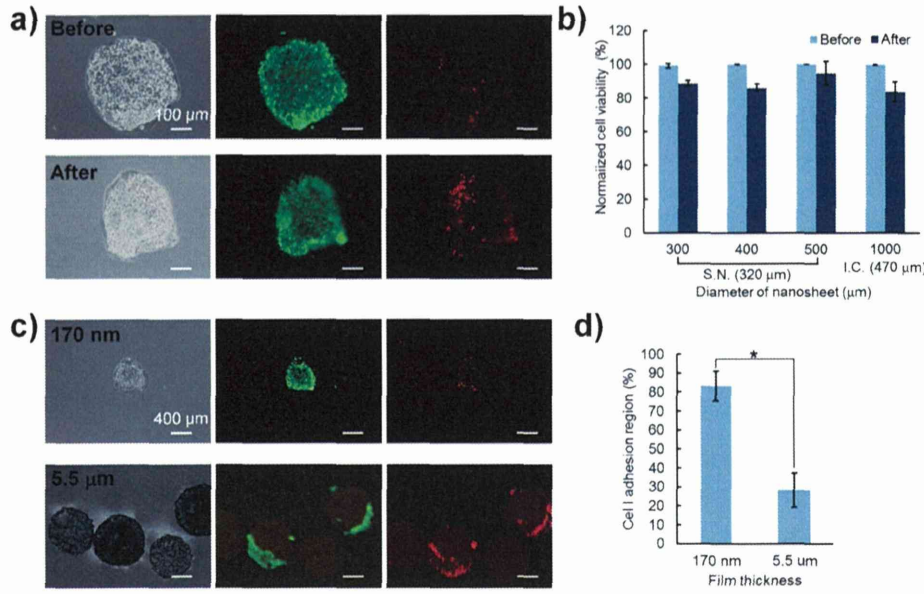

Figure 3. Evaluation of cell viability following syringe manipulation. a) Comparison of cell viability before and after injection of micropatterned nanosheets (400 μm ϕ) using a 25 G syringe needle (320 μm inner diameter). All scale bars indicate 100 μm. b) Quantification of cell viability on micropatterned nanosheets of different diameters. A 25 G syringe needle (S.N.) was used for nanosheets of 300 to 500 μm diameter, and a 24 G intravenous catheter (I.C.) was used for nanosheets of 1000 μm (the diameter of each needle is indicated below the Figure). c) Mechanical stability of cellular organization on micropatterned nanosheets (400 μm ϕ) of 170 nm or 5.5 μm thickness (all scale bars indicate 400 μm). d) Quantification of the cell adhesion region after syringe manipulation. Student's *t*-test with $^*p < 0.05$ set as the level of statistical significance.

This level of increase in roughness is consistent with that found in our previous study using polylactide nanosheets modified by MNPs.[10a] We compared the proliferation of RPE-J cells on nanosheets with and without MNPs and found that a significantly enhanced rate of proliferation occurred after 1 d of culture on the surface with MNPs (Figure 2d, $p < 0.05$). Immunohistochemical analysis of the morphogenesis in the RPE monolayer after 2 d of culture showed that cells on the surface with MNPs had a hexagonal structure with abundant formation of tight junctions, as visualized by the presence of the tight junction protein ZO-1 (Figure 2e); by contrast, cells on surfaces without MNPs were randomly organized (Figure 2f). Stress fibers (F-actin) formed along the tight junctions in cells on the surface with MNPs, but were less organized on cells on surfaces without MNPs. After 7 d of culture, the formation of tight junctions had occurred on both surfaces (data not shown). A previous study reported that cells grown on a nanoparticle-modified surface showed an increased area of contiguous contact of the cell membrane (endothelial cells) with the underlying substrate, and also showed a consistent increase in growth of F-actin filaments.[13a] Therefore, we anticipated that the greater surface roughness generated by MNPs would enhance cell migration and proliferation, and result in faster maturation of tight junctions in the epithelial monolayer. With regard to use of RPE cells in clinical applications, such enhanced morphogenesis on a micropatterned nanosheet would accelerate the process of transplantation of RPE monolayers.

On the assumption that transplantation of engineered RPE monolayers would be carried out using conventional syringe needles, we evaluated cell viability following mechanical compression of the micropatterned nanosheets inside a syringe needle that had a circular opening. The stability and viability of the RPE monolayer was evaluated on micropatterned nanosheets with different diameters by analyzing the cells after live/dead staining. After 2 d of culture, the cell/nanosheet constructs were detached from the glass substrate by gently scratching and rubbing the corner of the nanosheets. Due to the magnetic properties of the nanosheets, the freely suspended cell–nanosheet constructs could be remotely gathered in one place using an external magnetic force (Movie S2, Supporting Information); this enabled a minimally invasive collection of the engineered RPE monolayer. Each construct was then aspirated and injected through a 25 G syringe needle (320 μm inner diameter) at 10 mL min^{-1}. Despite the mechanical stress during syringe manipulation, the RPE monolayer retained its original shape without distortion (**Figure 3**a). Following cell staining, we estimated a rate of cell viability of over 80% for nanosheets ranging in diameter from 300 to 500 μm (Figure 3b). The ratio of the diameter of the nanosheet to that of the syringe needle was crucial for minimizing cell mortality during the manipulation process. If the inner diameter was increased, as in switching from a 25 G syringe needle (320 μm) to a 24 G intravenous catheter (470 μm), a micropatterned nanosheet of 1000 μm diameter could be injected without significant loss of cell viability (more than 85%) (see also Figure S5). These results suggest that the micropatterned nanosheet can withstand deformation in syringe needles with an internal diameter up to half that of the nanosheet. Furthermore, we also evaluated the effect of the thickness of the nanosheet on cell viability following syringe manipulation. Micropatterned nanosheets with

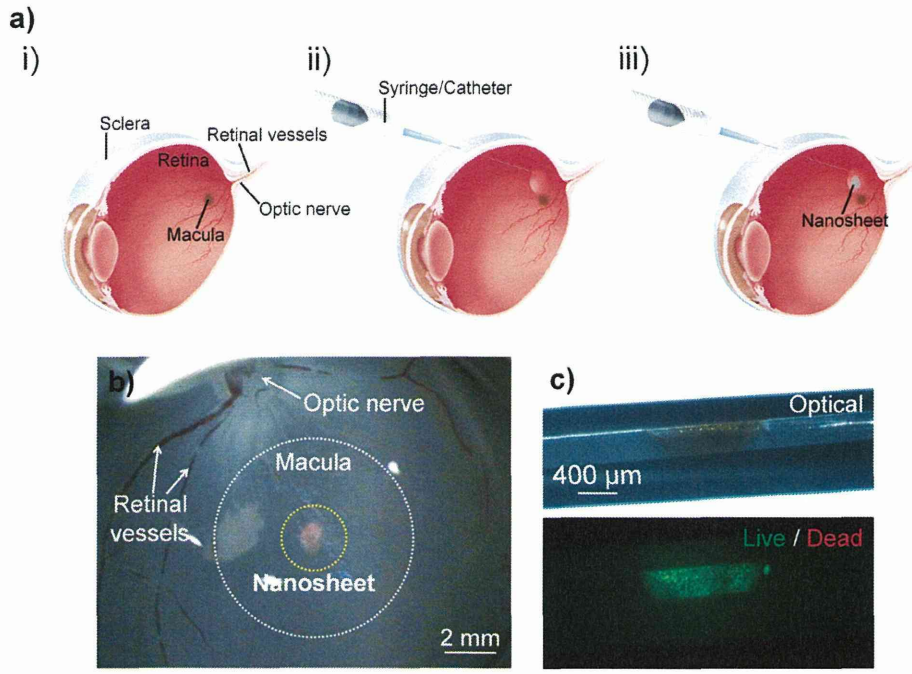

Figure 4. Injection of a micropatterned nanosheet into the subretinal space of a swine eye ex vivo. a) Schematic representation of the injection process: i) fresh swine eyeball without the detachment of retinal tissue, ii) subretinal injection of saline to make a space for injection, and, iii) injection of the micropatterned nanosheet (1000 μm ϕ) using a 24 G intravenous catheter (470 μm in inner diameter). b) Microscopic image of the injected nanosheet (stained with rhodamine B), which was fixed on the macula after removal of the saline. c) Staining of the micropatterned nanosheet with RPE-J cells in the catheter to show live/dead cells.

thicknesses of a few hundred of nanometers (170 nm) retained viable cells on the surface, whereas those that were micrometers in thickness (5.5 μm) retained few cells, with most showing low viability (Figure 3c). We assumed that cells on the latter nanosheets had been scraped from the surface during manipulation, resulting in only a few cells remaining. Such phenomena would be explained from the feasible elastic properties between cells and the 170 nm-thickness nanosheets rather than the 5.5 μm-thickness sheets; the more flexible substrate could retain the cellular organization under the mechanical stress. Indeed, comparison of the sizes of the cell adhesion regions showed that the thicker nanosheets had a significantly reduced area (Figure 3d). Overall, therefore our findings show that the ultrathin flexible structure of the micropatterned nanosheets is beneficial for aspirating them into a narrow space, such as a syringe needle, and also reduces the mechanical stress on the attached cells.

Finally, we used our system to deliver micropatterned nanosheets to the subretinal space of a swine eye ex vivo. Before injection of the nanosheet, the subretinal space was partially filled with saline in order to secure the transplanted site (**Figure 4**a). As the macula of the swine ocular ball is large, we injected a 1000 μm ϕ micropatterned nanosheet using a 24 G intravenous catheter. The nanosheet was successfully injected and spread into the subretinal space (see Movie S3, Supporting Information); it then attached to the macula and retained its circular shape after removal of the saline (Figure 4b). In addition, staining for live/dead cells showed that the RPE monolayer was stable inside the catheter needle and retained cellular activity (Figure 4c). Thus, the ex vivo results confirm the practicality of using micropatterned nanosheets for delivering an RPE monolayer in a therapeutic context. In this ex vivo study, the fixation of the cell monolayer after injection was facilitated by removal of the prefilled saline, since the native RPE layer is closely sandwiched between the retinal photoreceptors and the choroid. Thus, removal of the saline would be sufficient to fix the transplanted RPE monolayer stably. In addition, the number of cells on the nanosheet is basically adjustable in line with the AMD size. Therefore, it may be possible to inject multiple nanosheets through the syringe needle unless the prefilled saline is removed from the subretinal place. Such multiple injections would enhance the transplantation efficacy.

It was previously reported that polylactide nanosheets from 20 to 200 nm thick degraded within 1 week under physiological enzymatic conditions and also showed minimal inflammatory response in vivo due to the small amount of polymer.[14] For further estimation, we are currently investigating the biodegradability of the micropatterned nanosheets by using model eye fluid, such as aqueous humor (data not shown). In addition, it has recently been reported that MNP-labeled cells can be transplanted into rat retina without inducing a significant inflammatory response.[15] Thus, we incorporated MNPs or fluorescent dyes into the micropatterned nanosheets in order to visualize the structure, improve the ease of manipulation, and enhance cellular morphogenesis. Moreover, these materials can be substituted by other chemicals. For example,

fluorescein can be used as a dye since it is clinically available. The roughness effect induced by MNP could also be recapitulated by integrating microfabricated structure in the nanosheet (e.g., micropores or nano/microcues). Similar techniques could also be used to incorporate the drugs necessary for further improving the function of the nanosheet, that will be applied for drug delivery system.[16] For example, it may be possible to enhance the tissue integration of the transplanted RPE monolayer through the controlled release of drugs and growth factors from the micropatterned nanosheet. Thus, the micropatterned nanosheet will not only be of value for retaining cellular organization but also for enhancing cellular activity such as proliferation and differentiation. For further characterization of the tissue function, we are currently investigating transepithelial electrical resistance (TER) of the engineered RPE monolayer on the nanosheet using a volt–ohm meter.[13b] In addition, integration of the engineered tissue to the host tissue will be examined by histological analysis in vivo.

With respect to the clinical treatment of AMD using stem cells, such as induced pluripotent stem (iPS) cells,[17] it should be noted that the present technique for directing transplanted cells using micropatterned nanosheets may also be applicable for differentiated RPE cells from stem cells providing they adhere to the nanosheet. In particular, transplanted cells might induce apoptosis unless they attach correctly to the basement membrane;[18] the rate of attachment may depend on the anatomy and physiology of the basement membrane. In this regard, a micropatterned nanosheet may offer a good microenvironment for transplanted cells since the high flexibility of the nanosheet permits the stable attachment of the RPE monolayer despite the complicated surface of the retinal lesion. In addition, conventional cell-sheet engineering has to wait for cell confluence in order to detach the cells as a freestanding structure.[19] To this end, the nanosheets will provide stable platforms for the cells, on which the organized cells can be detached even without waiting for the cell maturation. Therefore, integration of the nanosheet technology into cell-sheet engineering may reduce the cell culture period and also enhance the overall transplantation process.

In summary, we described the development of micropatterned nanosheets that consisted of biodegradable PLGA and MNPs toward local delivery of RPE cells for the treatment of AMD. The micropatterned nanosheets promoted the formation of a stable monolayer of the RPE-J cells that could differentiate into a cobblestone-like structure. Owing to the high flexibility of the nanosheet, the RPE monolayer could be injected through a clinical syringe without significant loss of cell viability. We also injected micropatterned nanosheets into the subretinal space of a swine eye and showed that they could attach stably to the macula. Our results indicate that micropatterned nanosheets are useful substrates not only for delivery of RPE-J cells but also for enhancing morphogenesis in the cells, such as monolayer formation with hexagonal tight junctions. Furthermore, manipulability by magnetic force would be exploited for the minimally invasive delivery of the engineered RPE-J cells. In order to further improve cell transplantation methods, such as those for iPS cells, development of cell resources as well as effective delivery technique will play an important role for the enhancement of therapeutic efficacy. Flexible micropatterned nanosheets hold great promise for transplantation of organized cellular structures and for the development of local cell delivery systems.

Experimental Section

Experimental details are described in the Supporting Information.

Supporting Information

Supporting Information is available from the Wiley Online Library or from the author.

Acknowledgements

The authors thank Dr. Hao Liu and Prof. Ken Nakajima (WPI-AIMR, Tohoku University) for the AFM analysis. This work was supported by the World Premier International Research Center Initiative (WPI) and JSPS KAKENHI (grant number 25870050 for T.F., and 23681027 and 24651156 for H.K.) from MEXT, Japan, and the 5th Mandom International Research Grants on Alternative to Animal Experiments (H.K.).

Received: August 20, 2013
Revised: September 17, 2013
Published online: December 4, 2013

[1] S. R. Hynes, E. B. Lavik, *Graefes. Arch. Clin. Exp. Ophthalmol.* **2010**, *248*, 763.
[2] S. Binder, B. V. Stanzel, I. Krebs, C. Glittenberg, *Prog. Retin. Eye Res.* **2007**, *26*, 516.
[3] a) T. Abe, M. Yoshida, Y. Yoshioka, R. Wakusawa, Y. Tokita-Ishikawa, H. Seto, M. Tamai, K. Nishida, *Prog. Retin. Eye Res.* **2007**, *26*, 302; b) T. Abe, Y. Saigo, M. Hojo, T. Kano, R. Wakusawa, Y. Tokita, M. Tamai, *Cell Transplant.* **2005**, *14*, 799; c) Y. Saigo, T. Abe, M. Hojo, H. Tomita, E. Sugano, M. Tamai, *Invest. Opthalmol. Vis. Sci.* **2004**, *45*, 1996.
[4] a) A. Khademhosseini, R. Langer, J. Borenstein, J. P. Vacanti, *Proc. Natl. Acad. Sci. USA* **2006**, *103*, 2480; b) A. Khademhosseini, J. P. Vacanti, R. Langer, *Sci. Am.* **2009**, *300*, 64; c) N. E. Vrana, P. Lavalle, M. R. Dokmeci, F. Dehghani, A. M. Ghaemmaghami, A. Khademhosseini, *Tissue Eng. B Rev.* **2013** DOI: 10.1089/ten.teb.2012.0603.
[5] a) G. Thumann, A. Viethen, A. Gaebler, P. Walter, S. Kaempf, S. Johnen, A. K. Salz, *Biomaterials* **2009**, *30*, 287; b) S. Tao, C. Young, S. Redenti, Y. Zhang, H. Klassen, T. Desai, M. J. Young, *Lab Chip* **2007**, *7*, 695; c) B. V. Stanzel, Z. Liu, R. Brinken, N. Braun, F. G. Holz, N. Eter, *Invest. Opthalmol. Vis. Sci.* **2012**, *53*, 490.
[6] J. A. Forrest, K. Dalnoki-Veress, *Adv. Colloid Interface Sci.* **2001**, *94*, 167.
[7] T. Fujie, Y. Okamura, S. Takeoka, in *Functional Polymer Films*, Vol. *2* (Eds: W. Knoll, R. C. Advincula), Wiley-VCH, Weinheim, Germany **2011**, p. 907.
[8] a) T. Fujie, Y. Okamura, S. Takeoka, *Adv. Mater.* **2007**, *19*, 3549; b) T. Fujie, N. Matsutani, M. Kinoshita, Y. Okamura, A. Saito, S. Takeoka, *Adv. Funct. Mater.* **2009**, *19*, 2560; c) T. Fujie, S. Furutate, D. Niwa, S. Takeoka, *Soft Matter* **2010**, *6*, 4672.
[9] a) T. Fujie, L. Ricotti, A. Desii, A. Menciassi, P. Dario, V. Mattoli, *Langmuir* **2011**, *27*, 13173; b) T. Fujie, A. Desii, L. Ventrelli, B. Mazzolai, V. Mattoli, *Biomed. Microdevices* **2012**, *14*, 1069.

[10] a) S. Taccola, A. Desii, V. Pensabene, T. Fujie, A. Saito, S. Takeoka, P. Dario, A. Menciassi, V. Mattoli, *Langmuir* **2011**, *27*, 5589; b) T. Fujie, S. Ahadian, H. Liu, H. Chang, S. Ostrovidov, H. Wu, H. Bae, K. Nakajima, H. Kaji, A. Khademhosseini, *Nano Lett.* **2013**, *13*, 3185.

[11] a) T. Fujie, Y. Kawamoto, H. Haniuda, A. Saito, K. Kabata, Y. Honda, E. Ohmori, T. Asahi, S. Takeoka, *Macromolecules* **2013**, *46*, 395; b) B. Eling, S. Gogolewski, A. J. Pennings, *Polymer* **1982**, *23*, 1587.

[12] a) A. R. Harris, L. Peter, J. Bellis, B. Baum, A. J. Kabla, G. T. Charras, *Proc. Natl. Acad. Sci. USA* **2012**, *109*, 16449; b) C. Guillot, T. Lecuit, *Science* **2013**, *340*, 1185.

[13] a) A. M. Lipski, C. J. Pino, F. R. Haselton, I. W. Chen, V. P. Shastri, *Biomaterials* **2008**, *29*, 3836; b) K. R. Kam, L. A. Walsh, S. M. Bock, M. Koval, K. E. Fischer, R. F. Ross, T. A. Desai, *Nano Lett.* **2013**, *13*, 164.

[14] a) Y. Okamura, K. Kabata, M. Kinoshita, D. Saitoh, S. Takeoka, *Adv. Mater.* **2009**, *21*, 4388; b) K. Fujino, M. Kinoshita, A. Saitoh, H. Yano, K. Nishikawa, T. Fujie, K. Iwaya, M. Kakihara, S. Takeoka, D. Saitoh, Y. Tanaka, *Surg. Endosc.* **2011**, *25*, 3428; c) Y. Okamura, K. Kabata, M. Kinoshita, H. Miyazaki, A. Saito, T. Fujie, S. Ohtsubo, D. Saitoh, S. Takeoka, *Adv. Mater.* **2013**, *25*, 545.

[15] A. Yanai, U. O. Häfeli, A. L. Metcalfe, P. Soema, L. Addo, C. Y. Gregory-Evans, K. Po, X. Shan, O. L. Moritz, K. Gregory-Evans, *Cell Transplant.* **2012**, *21*, 1137.

[16] a) T. Fujie, A. Saito, M. Kinoshita, H. Miyazaki, S. Ohtsubo, D. Saitoh, S. Takeoka, *Biomaterials* **2010**, *31*, 6269; b) A. Saito, H. Miyazaki, T, Fujie, S. Ohtsubo, M. Kinoshita, D. Saitoh, S. Takeoka, *Acta Biomater.* **2012**, *8*, 2932; c) K. Kashiwagi, K. Ito, H. Haniuda, S. Ohtsubo, S. Takeoka, *Invest. Opthalmol. Vis. Sci.* **2013**, *54*, 5629.

[17] a) K. Takahashi, S. Yamanaka, *Cell* **2006**, *126*, 663; b) T. Kuroda, S. Yasuda, S. Kusakawa, N. Hirata, Y. Kanda, K. Suzuki, M. Takahashi, S. Nishikawa, S. Kawamata, Y. Sato, *PLoS One* **2012**, *7*, e37342; c) D. Cyranoski, *Nature* **2013**, *494*, 413.

[18] a) L. V. Del Priore, T. H. Tezel, *Arch. Ophthalmol.* **1998**, *116*, 335; b) T. H. Tezel, L. V. Del Priore, *Invest. Ophthalmol. Vis. Sci.* **1999**, *40*, 767.

[19] a) N. Matsuda, T. Shimizu, M. Yamato, T. Okano, *Adv. Mater.* **2007**, *19*, 3089; b) H. Takahashi, M. Nakayama, M. Yamato, T. Okano, *Biomacromolecules* **2010**, *11*, 1991.

Doc Ophthalmol (2015) 130:149–156
DOI 10.1007/s10633-014-9478-2

ORIGINAL RESEARCH ARTICLE

Molecular, anatomical and functional changes in the retinal ganglion cells after optic nerve crush in mice

Masayoshi Yukita · Shigeki Machida · Koji M. Nishiguchi · Satoru Tsuda · Yu Yokoyama · Masayuki Yasuda · Kazuichi Maruyama · Toru Nakazawa

Received: 21 October 2014 / Accepted: 30 December 2014 / Published online: 6 January 2015

Abstract
Purpose Optic nerve crush (ONC) and subsequent axonal damage can be used in rodents to study the mechanism of retinal ganglion cell (RGC) degeneration. Here, we examined electroretinograms (ERGs) in post-ONC mice to investigate changes in the positive scotopic threshold response (pSTR). We then compared these changes with molecular and morphological changes to identify early objective biomarkers of RGC dysfunction.
Methods Fifty 12-week-old C57BL/6 mice were included. ONC was used to induce axonal injury in the right eye of each animal, with the left eye used as a control. The expression of the RGC markers *Brn3a* and *Brn3b* was measured on days 1, 2, 3, 5 and 7 after ONC with quantitative real-time PCR. ERGs were recorded under dark adaptation with the stimulus intensity increasing from −6.2 to 0.43 log cd-s/m^2 on days 1, 2, 3, 5, 7 and 10 after ONC. The pSTR, a- and b-wave amplitudes were measured. Inner retinal thickness around the optic nerve head was measured with spectral-domain optical coherence tomography on days 0, 2, 5, 7 and 10 after ONC.
Results The expression of *Brn3a* and *Brn3b* began to significantly decrease on day 1 and day 2, respectively ($P < 0.01$). The amplitude of the pSTR underwent rapid, significant deterioration on day 3, after which it fell gradually ($P < 0.01$), while the a- and b-wave amplitudes remained unchanged throughout the experiment. Inner retinal thickness gradually decreased, with the most significant reduction on day 10 ($P < 0.01$).
Conclusions Decrease in pSTR likely reflected the early loss of RGC function after ONC and that declining expression of RGC-specific genes preceded anatomical and functional changes in the RGCs.

M. Yukita · S. Tsuda · Y. Yokoyama · M. Yasuda · K. Maruyama · T. Nakazawa (✉)
Department of Ophthalmology, Tohoku University Graduate School of Medicine, 1-1 Seiryo, Aoba, Sendai, Miyagi 980-8574, Japan
e-mail: ntoru@oph.med.tohoku.ac.jp

S. Machida
Department of Ophthalmology, Dokkyo Medical University Koshigaya Hospital, Saitama, Japan

S. Machida
Department of Ophthalmology, Iwate Medical University School of Medicine, Morioka, Japan

K. M. Nishiguchi · T. Nakazawa
Department of Advanced Ophthalmic Medicine, Tohoku University Graduate School of Medicine, Sendai, Miyagi, Japan

T. Nakazawa
Department of Retinal Disease Control, Tohoku University Graduate School of Medicine, Sendai, Miyagi, Japan

Keywords Axonal injury · Glaucoma · Retinal ganglion cell · Electroretinogram · Scotopic threshold response

Introduction

Currently available treatments for glaucoma mostly depend on lowering intraocular pressure (IOP) [1]. However, even after the successful reduction in IOP, visual dysfunction continues to progress in many glaucoma patients [2], likely due to the influence of IOP-independent contributing factors [1–3] such as axonal injury [2]. Thus, new therapies targeting these factors have been the subject of recent research and development.

Animal models are one of the most useful tools for understanding the pathogenesis of disease and developing new treatments. Research on retinal ganglion cell (RGC) degeneration commonly uses optic nerve crush (ONC) in rodents as an animal model [4, 5]. However, despite numerous previous studies of ONC-induced morphological and molecular changes in the RGCs [6, 7], early sequential change in RGC function, especially its relationship with alterations in gene expression, remains poorly understood.

The photopic negative response (PhNR) [8] of the photopic electroretinogram (ERG) has emerged as a new functional measure of the RGCs in clinical practice [9–14]. However, studies have suggested that, in rodents, the PhNR originates from amacrine cells [15] and is thus unaffected by ONC [15, 16]. A useful alternative may be the scotopic threshold response (STR) of the scotopic ERG, which is elicited by very dim stimuli and is driven by the inner retina, including the RGCs [17, 18]. The STR consists of negative and positive components, defined as the positive STR (pSTR) and negative STR (nSTR), respectively [16]. In particular, the pSTR has been suggested to reflect RGC function in rodents [16, 19, 20]. However, it has not been determined at what time point after ONC alterations begin to occur in the pSTR caused by the functional loss of RGCs.

The aim of this study was therefore to determine whether the pSTR could serve as an early biomarker of RGC dysfunction after ONC in mice. We thus set out to compare changes in the pSTR with molecular and morphological changes in the RGCs after ONC.

Methods

Animals

Fifty C57BL/6 mice (male, 12-week-old; SLC, Hamamatsu, Japan) were used in this study. All animals were handled in accordance with the guidelines of the ARVO Statement for the Use of Animals in Ophthalmic and Vision Research and the guidelines from the Declaration of Helsinki. All experimental procedures described were approved by the Ethics Committee for Animal Experiments of Tohoku University Graduate School of Medicine.

During the surgical procedures, recording of the ERGs and spectral-domain optical coherence tomography (SD-OCT) imaging, the mice were anesthetized with ketamine (100 mg/kg) and xylazine (9 mg/kg). In the ONC procedure, the optic nerve was exposed, crushed 1.0 mm posterior to the globe with fine forceps for 5 s and released [4]. This procedure was performed by a single surgeon in order to reduce variations in the severity of the ONC-induced damage. The contralateral eye was left untouched and served as a control.

Quantitative real-time PCR

Total RNA (200 ng per sample) extracted from the retina was first reverse transcribed into cDNA using SuperScript III (Invitrogen Life Technologies, Carlsbad, CA, USA). Quantitative real-time PCR (RT-PCR) was then performed in duplicate with a 7500 Fast RT-PCR System (Applied Biosystems, Foster City, CA, USA) as previously described [21]. To determine relative gene expression, we analyzed the RT-PCR data with the comparative Ct method ($2^{-\Delta\Delta CT}$), normalized to an

Table 1 List of Taqman probes used in this study

Gene symbol	Assay ID
Pou4f1	Mm02343791_m1
Pou4f2	Mm00454754_s1

endogenous control (*Gapdh*). The Taqman probes used for these reactions are listed in Table 1.

Recording the ERG

The mice were dark-adapted overnight and were prepared for the ERG recording under dim red light. Each animal underwent additional dark adaptation for approximately 30 min before starting the ERG recording. The mice were anesthetized with an intraperitoneal injection of a mixture of ketamine (100 mg/kg) and xylazine (10 mg/kg).

The pupils were maximally dilated with topical 0.5 % tropicamide and 0.5 % phenylephrine HCL, and the corneas were anesthetized with topical 0.4 % oxybuprocaine hydrochloride. A contact lens electrode embedded with gold wire was placed on the cornea as an active electrode (Mayo, Nagoya, Japan), and a chloride silver plate was placed in the mouth as a reference electrode. A grounded aluminum sheet placed under the animal served as the ground electrode. Body temperature was kept at 37 °C with a heating pad.

The ERGs were recorded from both eyes simultaneously using a Ganzfeld bowl that had originally been assembled at the Kellogg Eye Center (Ann Arbor, MI, USA). Responses were amplified 10,000 times and band-pass filtered from 0.3 to 500 Hz (PuREC PC-100, Mayo, Inazawa, Japan). Brief white stimuli were produced by a xenon arc lamp that was mounted on the top of the Ganzfeld bowl and controlled by a photic stimulator (PS33-PLUS, Grass Instruments, Quincy, MA, USA). The ERG was recorded under dark adaptation with increasing stimulus intensity from −6.2 to 0.43 log cd-s/m^2 in 0.40-, 0.23- or 0.37-log-unit steps. The flash duration was 10 μs. The response to approximately 20–30 flashes was recorded at each stimulus intensity, with an inter-stimulus interval of 3 s, and then averaged to determine the final value of the STR [16, 22, 23]. The pSTR and nSTR amplitudes were measured from the baseline to the peak of the first positive wave and from the baseline to the negative trough after the positive wave, respectively (Fig. 2a). In higher stimulus ranges, 2–3 responses were averaged with an inter-stimulus interval of 10–60 s, depending on the stimulus intensity. The a-wave amplitude was measured from the baseline to the trough of the first negative response and the b-wave amplitude from the first trough to the peak of the following positive wave.

SD-OCT imaging

After pupil dilation, hydroxymethylcellulose (Goniosol, 2.5 %; Alkon, Buffalo Grove, IL, USA) was applied to the cornea during the recording. Retinal images were then acquired by scanning circumferentially around the optic nerve head with spectral-domain optical coherence tomography (SD-OCT) (RS-3000 Advance, Nidek). The distance between the internal limiting membrane and inner plexiform layer was measured to determine inner retinal thickness.

Statistical analysis

A one-way repeated-measures ANOVA with a post hoc Bonferroni test was used to assess the post-ONC quantitative RT-PCR data. A two-way repeated-measures ANOVA with a post hoc Bonferroni test was used to compare the OCT data in the control and ONC eyes. A paired Student *t* test was performed to compare the STR amplitude in the control and ONC eyes. Average values are shown as the mean with standard error. Differences were considered significant at $P < 0.05$.

Results

Reduced RGC-specific gene expression after ONC

Functional and morphological changes in the RGCs likely accompany changes in RGC-specific gene expression. We therefore used RT-PCR to determine the time when generalized changes in gene expression took place in the RGCs following ONC. This was done by studying the temporal expression profile of two representative RGC-specific genes: *Brn3a* and *Brn3b,* which have been shown to represent defferent RGC types (Fig. 1). [24, 25] *Brn3a* showed the earliest decrease in expression, on day 1 (40.9 ± 13.4 % reduction, Bonferroni test, $P < 0.01$). This was followed by a decrease in *Brn3b* (65.9 ± 8.9 % reduction, Bonferroni test, $P < 0.01$) on day 2.

Intensity–response function after ONC

Figure 2 shows representative intensity–response series of the scotopic ERG for the control (black line) and ONC (red line) eyes on days 1 and 10. On day 1,

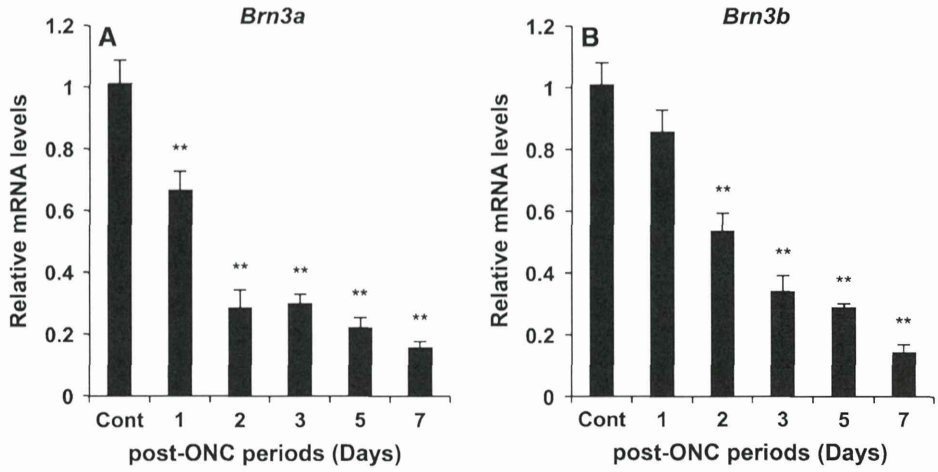

Fig. 1 The retinal mRNA levels of *Brn3a* (**a**) and *Brn3b* (**b**) were measured on days 1, 2, 3, 5, and 7 after ONC ($n = 6$ at each time point). There was a significant reduction in gene expression on day 1 for *Brn3a* and on day 2 for *Brn3b*. *ONC* optic nerve crush, *error bars* standard error, $^{**}P < 0.005$

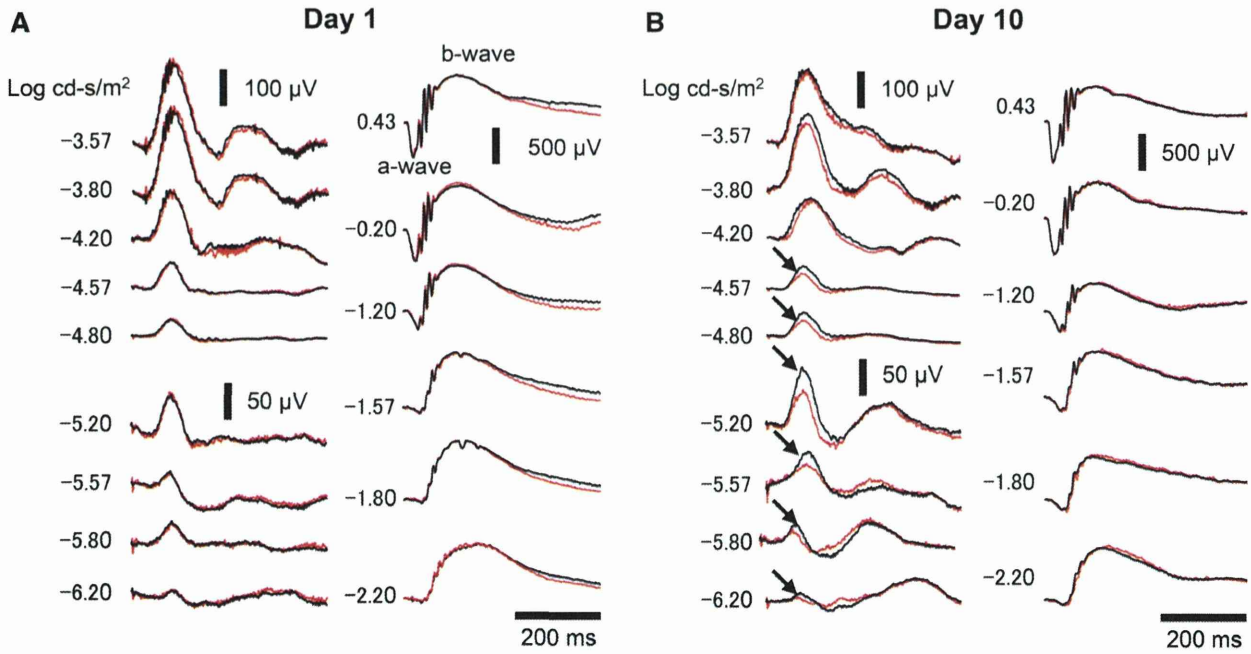

Fig. 2 Representative intensity–response ERG series recorded from control (*black lines*) and ONC (*red lines*) eyes on days 1 (**a**) and 10 (**b**) after ONC. The pSTR to low-intensity stimuli in the ONC eyes deteriorated on day 10 (indicated by the *arrows* in **b**). *ERG* electroretinogram, *ONC* optic nerve crush, *pSTR* positive scotopic threshold response

the waveforms completely overlapped over the entire stimulus range. On day 10, the pSTR in the lower stimulus range deteriorated in the ONC eyes relative to the control eyes (indicated by the arrows in Fig. 2b). The a- and b-waves of the control and ONC eyes elicited by stimuli of higher intensities completely overlapped. As there was no significant difference in the nSTR amplitude of the treated and untreated eyes at any stimulus intensity, we excluded nSTR results from our analysis.

The amplitude of the positive waves, including the pSTR and b-waves, was plotted against stimulus intensity to determine the intensity–response function on days 1, 2, 3, 5, 7 and 10 after ONC for the control (black symbols) and ONC (red symbols) eyes (Fig. 3a–f). The a-wave amplitude is also shown in the lower right of each figure. The intensity–response curves of the control and ONC eyes overlapped until day 2. In the lower stimulus range, the curve of the ONC eyes shifted downward and separated from the

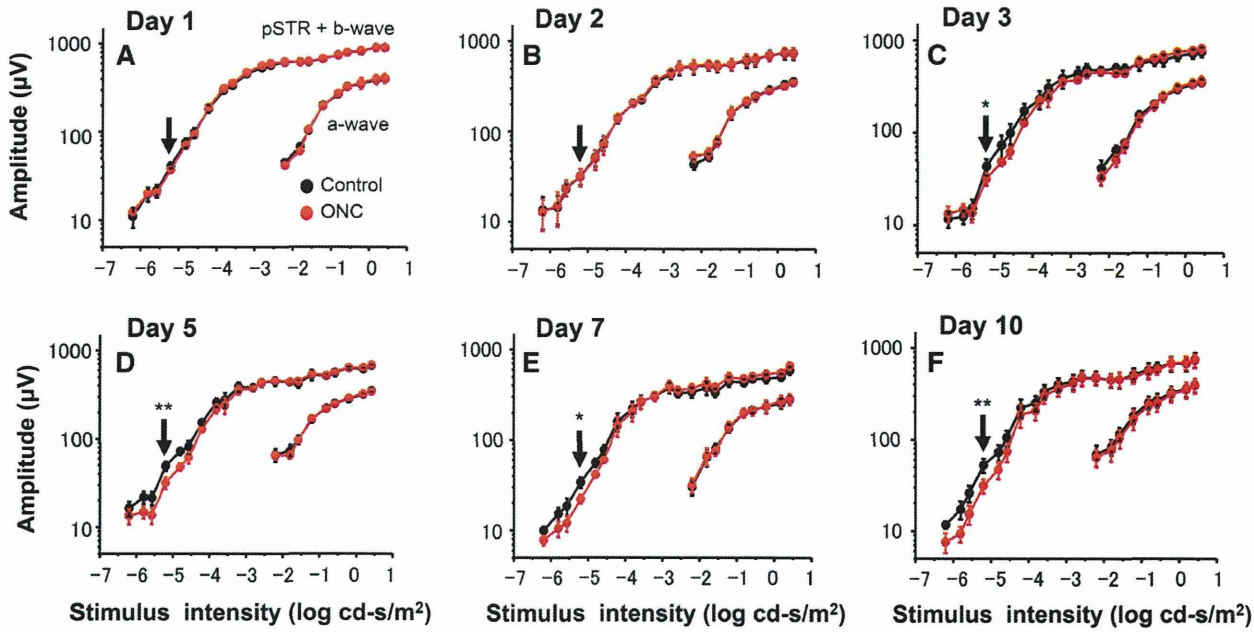

Fig. 3 Intensity–response functions for the pSTR + b-wave and a-waves recorded from control ($n = 5$, *black symbols*) and ONC ($n = 5$, *red symbols*) eyes on days 1 (**a**), 2 (**b**), 3 (**c**), 5 (**d**), 7 (**e**) and 10 (**f**) after ONC. The arrows in each figure indicate the pSTR amplitude elicited by a stimulus intensity of −5.2 log cd-s/m^2. *pSTR* positive scotopic threshold response, *ONC* optic nerve crush, *error bars* standard error, $*P < 0.01$, $**P < 0.005$

curve of the control eyes on day 3. On day 10, the maximum difference between the control and ONC eyes was seen, at the stimulus intensity of 5.2 log cd-s/m^2 (Fig. 3f). Therefore, subsequent analyses used the pSTR amplitude elicited at an intensity of −5.2 log cd-s/m^2 to compare the control and ONC eyes (indicated by the arrows in Fig. 3). Significant differences were seen in the pSTR amplitude between the control and ONC eyes after day 3 (paired *t* test, $P < 0.01$ for days 3 and 7; $P < 0.005$ for days 5 and 10).

Inner retinal thickness after ONC, measured with in vivo OCT imaging

Finally, we measured the thickness of the inner retina around the optic nerve head, as a morphological indicator of the status of the RGCs on days 1, 2, 3, 5, 7 and 10 after ONC (Fig. 4b). Figure 4b shows a representative OCT image, obtained on day 10, in which the selective loss of the inner retina is visible. After day 5, the inner retinal thickness gradually and progressively declined, with the most significant difference between the control and ONC eyes being seen on day 10 (Fig. 4c, Bonferroni test, $P < 0.01$).

Correlation between pSTR and inner retinal thickness

The pSTR amplitude and inner retinal thickness of the ONC eyes were normalized to those of the contralateral control eyes, expressed as a percentage and plotted as a function of the post-ONC period (Fig. 4d). A rapid loss in pSTR amplitude was seen on day 3, followed by a gradual loss over time, concurrent with the gradual loss of inner retinal thickness.

Discussion

In this study, we found that changes in the pSTR could be used to detect dysfunction of the RGCs as early as day 3 after ONC and that changes occurred in the pSTR earlier than in the OCT-measured morphology of the retina, which did not occur until day 10. Moreover, we previously used retrograde Fluorogold labeling of the RGCs to show that RGC loss began 5 days after ONC, suggesting that the alterations in the pSTR observed here occurred before even microscopic loss of the RGCs [4]. We have also previously found that in